Direct Numerical Simulation of a Spatially Evolving Supersonic Turbulent Boundary Layer at $Ma = 6$ *

LI Xin-Liang(李新亮)**, FU De-Xun(傅德薰), MA Yan-Wen(马延文)

LNM, Institute of Mechanics, Chinese Academy of Sciences, Beijing 100080

(Received 4 March 2006)

Direct numerical simulation is carried out for a spatially evolving supersonic turbulent boundary layer at free-stream Mach number 6. To overcome numerical instability, the seventh-order WENO scheme is used for the convection terms of Navier–Stokes equations, and fine mesh is adopted to minimize numerical dissipation. Compressibility effects on the near-wall turbulent kinetic energy budget are studied. The cross-stream extended self-similarity and scaling exponents including the near-wall region are studied. In high Mach number flows, the coherence vortex structures are arranged to be smoother and streamwised, and the hair-pin vortices are less likely to occur.

PACS: 47.27.Eq, 47.27.Nz, 83.85.pt

Direct numerical simulation (DNS) plays an important role in the study of turbulence. Until now, there have been a number of DNS studies on compressible boundary-layer turbulence.[1−6] In Refs. [1–3], the authors considered temporal DNS, whereas the authors of Ref. [4–6] studied spatial DNS. Compared to the temporal evolving one, the spatially evolving DNS does not need the 'slow growth' or 'extended temporal' assumptions, and thus uncertainty or artificial assumptions[5] can be minimized. Because of the numerical difficulty, there is still no report on DNS of spatially evolving turbulent boundary layer at high Mach number.

In this Letter, DNS of a spatially evolving turbulent boundary layer at free stream Mach number $Ma = 6$ is performed, and its statistical characteristics, near wall kinetic energy budget and cross-stream scaling law is discussed.

The flow parameters and mesh parameters in the present computation are listed in Table 1. Here Ma_∞ is the free stream Mach number; Re_∞ is the free stream Reynolds number (using one inch as the length unit); $Re_\theta = \rho_\infty u_\infty \theta/\mu_\infty$ is the Reynolds number based on the momentum thickness θ at $x = 9.8$ and free-stream velocity. $Re_\tau = \bar{\rho}_w u_\tau \theta/\bar{\mu}_w$ is the Reynolds number based on the momentum thickness θ and the wall friction velocity $u_\tau = \sqrt{\tau_w/\bar{\rho}_w}$ at $x = 9.8$.

Table 1. Computational parameters.

Ma_∞	Re_∞	T_w	Re_θ	Re_τ
6.0	2×10^6	6.98	1.095×10^5	265.0
$Nx \times Ny \times Nz$		$L_x \times L_y \times L_z$	$\Delta x^+ \times \Delta y_w^+ \times \Delta z^+$	
$4000 \times 90 \times 256$		$10 \times 0.59 \times 0.2$	$8.07 \times 0.97 \times 3.78$	

The convection terms in the compressible Navier–Stokes (N-S) equations are approximated by using the seventh-order WENO scheme,[7] the viscous terms are approximated by using the eighth-order central difference scheme, and the third-order TVD type Runge–Kutta method is used for time stepping.

Figure 1 shows the sketch of computational meshes. The mesh size in the x direction for uniform $x < 10.0$, whereas progressively coarsening grid at $x > 10.0$ is used as a buffer region to exhibit the reflection of numerical disturbance at the outlet boundary. Fine mesh is adopted near the wall, and uniform mesh is used in the spanwised direction. Total number of computational mesh is $4000 \times 90 \times 256$.

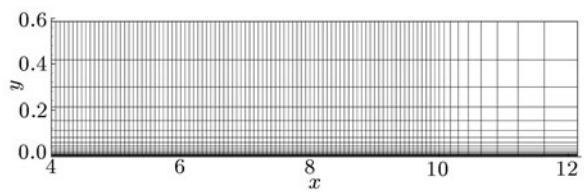

Fig. 1. Sketch of computational meshes.

A two-dimensional laminar flat-plate boundary layer including the leading edge is simulated, and the computed two-dimensional results at $x = 4.0$ are used as the inflow conditions for a downstream three-dimensional computation. Non-reflect boundary conditions are used at the upper boundary and outflow boundary. Blow and suction disturbance with amplitude $A = 0.2$ with a base frequency $\beta = 0.5$[5,6] are imposed at the wall in the interval $4.0 = x_a \le x \le x_b = 4.5$.

Figure 2 shows spanwised two-point correlations at $x = 9.8$ and $y^+ = 21.89$. We can see that the correlations decay toward zero with increasing distance between the two points. This means that the selected domain is wide enough in the spanwise direction.

Figure 3 shows the skin friction, defined as $C_f = \tau_w(\rho\bar{u}^2/2)$, $\tau_w = \mu_w \partial\bar{u}/\partial y|_w$, in the streamwise direction. It can be seen that the skin friction increases fast

* Supported by the National Natural Science Foundation of China under Grant Nos 90205025, 19872069, 170176033, and 10502052, and the Informatization Construction of Knowledge Innovation Projects of Chinese Academy of Sciences under Grant No INF105-SCE.

** Email: lixl@lnm.imech.ac.cn

in the transition region. Figure 4 shows the profiles of mean streamwised velocity $\bar{u}$ and the mean van Driest velocity $\bar{u}_{vd}$ normalized by the wall-shear velocity at $x = 9.8$. Because of the high wall temperature, the difference between $\bar{u}$ and $\bar{u}_{vd}$ is very large. The wall law and the log law expressed by $u^+ = 2.5 \ln y^+ + 5.9$ are found to be well satisfied.

The turbulence intensity profiles normalized by the local mean velocity at $x = 9.8$ are shown in Fig. 5, in which the symbols represent the experimental data for the corresponding incompressible flat-plate boundary. Form this figure we can see that the compressible and incompressible data are in good agreement with those in the near wall region $y^+ < 10$. The reason is that in the near wall region, the turbulent Mach number is low, and the compressibility effects are not considerable. In the region $y^+ > 20$, due to compressibility effects the normalized turbulence intensities are lower than the incompressible ones.

Figure 6 shows the profile of turbulent Mach number defined by $M_t = \sqrt{u'^2_{rms} + v'^2_{rms} + w'^2_{rms}}/\bar{c}$ at $x = 9.8$. From this figure we can see that the highest turbulent Mach number is greater than 0.4. This means that the intrinsic compressible effects are noticeable.

Figure 7 shows the Reynolds averaged and the Favre averaged temperature profiles at $x = 9.8$. The difference between the two profiles implies the intrinsic compressibility effects.

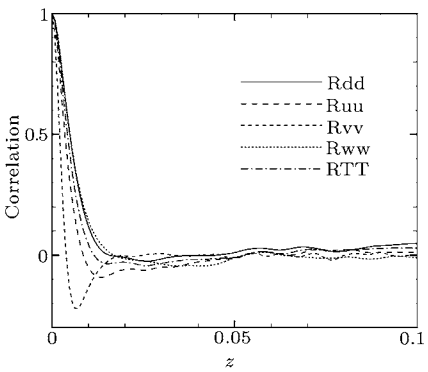

Fig. 2. Spanwised two-point correlations at $y^+ = 21.89$.

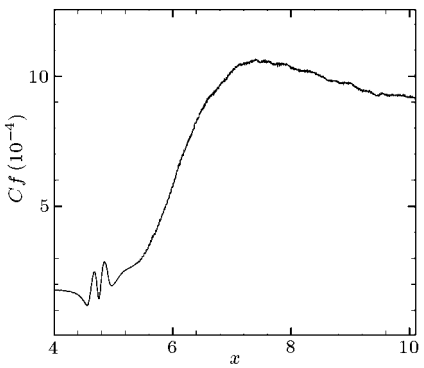

Fig. 3. Wall skin friction.

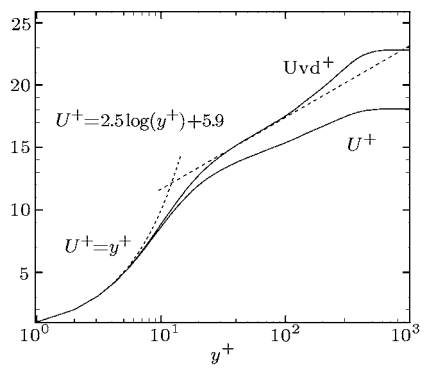

Fig. 4. Mean stream velocity and van Direst velocity.

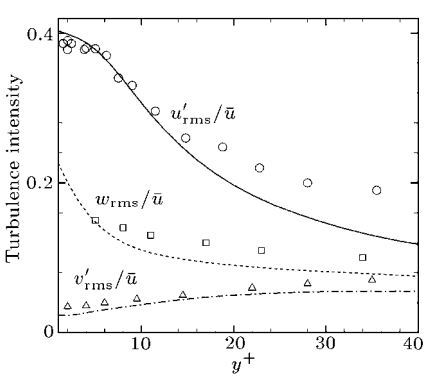

Fig. 5. Near wall normalized rms velocity (Symbols are the experimental data for impressible turbulent flow).

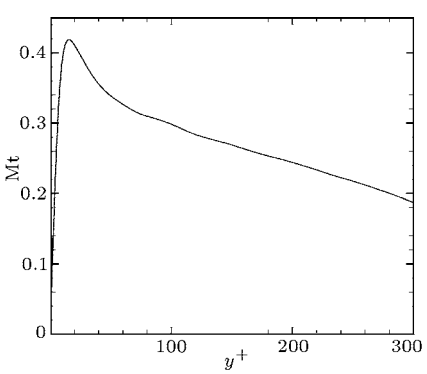

Fig. 6. Turbulent Mach number at $x = 9.8$.

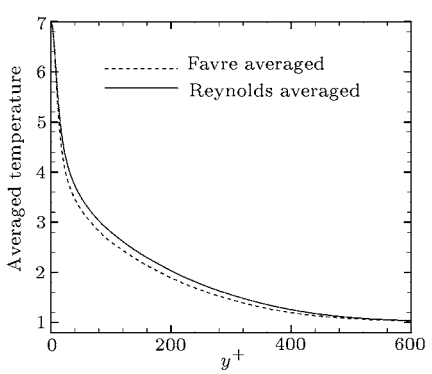

Fig. 7. Reynolds averaged and Favre averaged temperature at $x = 9.8$.

Figure 8 shows the mean velocity profiles $\bar{u} = \bar{u}(y)$ at different x locations. We can see that the mean velocity profiles have inflection points in the transition region, and then the inflection points disappear in the final stage of transition. The mean velocity profiles with inflection points lead to instability, and accelerate the transition. This agrees with the results of Ref. [8]. The second difference of mean velocity $d^2\bar{u}/dy^2$ is shown in Fig. 9, from which it can be clearly seen that there are inflection points with $d^2\bar{u}/dy^2 = 0$ in the mean velocity profiles at $x = 5.25$ and 5.86. The inflection points disappear at the downstream point $x = 6.92$.

The compressible turbulent kinetic energy equation reads

$$\frac{\partial}{\partial t}(\bar{\rho}K) = -C + P + T + \Pi_t + \Pi_d + D + M - \varepsilon,$$

where $C = \dfrac{\partial}{\partial x_j}(\tilde{u}_j \bar{\rho} K)$ is the convection term, $P = -\overline{\rho u_i'' u_j''}\partial \tilde{u}_i/\partial x_j$ is the production term, $T = -\dfrac{\partial}{\partial x_j}(1/2\overline{\rho u_i'' u_i'' u_j''})$ is the turbulent transport term, $\Pi_d = \overline{p'\partial u_i''/\partial x_i}$ is the pressure-dilatation term, $\Pi_t = -\partial(\overline{p' u_j''})/\partial x_j$ is the pressure transport term, $M = \bar{u}_i''(\partial \bar{\sigma}_{ij}/\partial x_j - \partial \bar{p}/\partial x_i)$ is the term associated with

density fluctuations, $D = \dfrac{\partial}{\partial x_i}\overline{u_i''\sigma_{ij}'}$ is the viscous diffusion term, $\varepsilon = \overline{\sigma_{ij}'\partial u_i''/\partial x_j}$ is the viscous dissipation term. In the above expressions, $\tilde{\phi} = \overline{\rho\phi}/\bar{\phi}$ is the Favre average of ϕ and $\phi' = \phi - \bar{\phi}$, $\phi'' = \phi - \tilde{\phi}$.

Figure 10 shows the turbulence kinetic energy budget at $x = 9.8$, and all the terms are normalized by the viscous dissipation term at the wall, i.e. ε_w. From this figure we can see that the turbulent energy production term P, the dissipation term ε, the turbulent transport term T and the viscous diffusion term D are dominant, and the other terms are small.

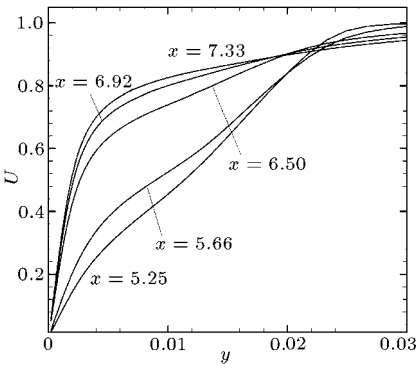

Fig. 8. Mean velocity profiles $\bar{u}$ at different x locations.

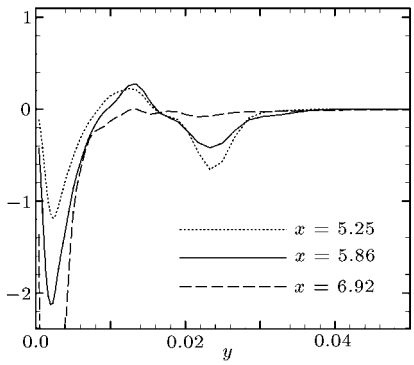

Fig. 9. Characteristics of $d^2\bar{u}/dy^2$ at different x locations.

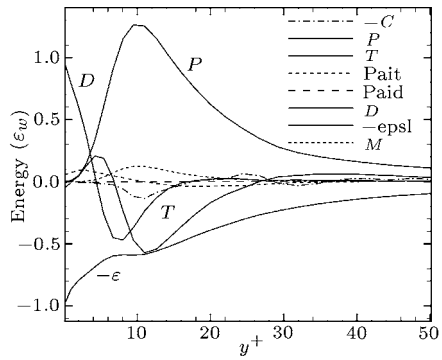

Fig. 10. Turbulence kinetic energy budget (normalized by ε_w) at $x = 9.8$.

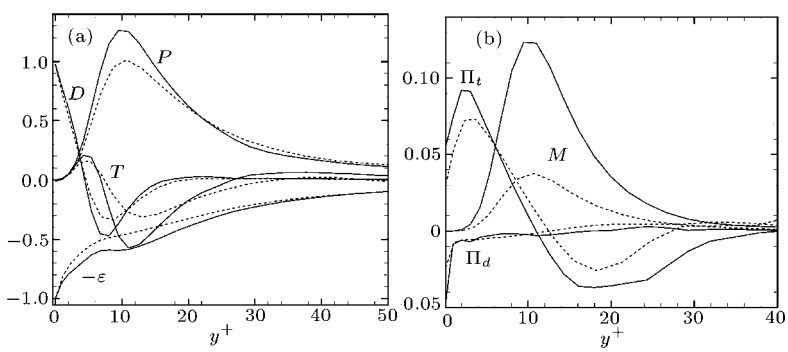

Fig. 11. Normalized turbulence kinetic energy budget for $Ma = 6$ (solid) and $Ma = 2.25$ (dashed).

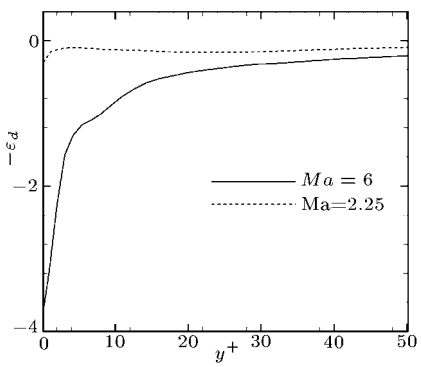

Fig. 12. Normalized dilatation dissipation.

Comparisons of the normalized turbulence kinetic energy budget at $Ma = 6$ and $Ma = 2.25$ are shown in Fig. 11, where the solid lines are the normalized kinetic energy for $Ma = 6$ at $x = 9.8$ and the dashed lines are the normalized kinetic energy for $Ma = 2.25$ at $x = 7.8$.[6] From Fig. 11(a) we can see that difference of the turbulent transport term, T, between the two Mach number cases is remarkable. Form Fig. 11(b) we see that the term associated with the density fluctuations (M term) for $Ma = 6$ is much higher than that for $Ma = 2.25$, resulting from the difference between the Reynolds average and Favre average at high Mach numbers, and the non-negligible term $\bar{u}_i''$. Figure 11(b) shows that the pressure-dilatation term Π_d for $Ma = 6$ is much higher than that for $Ma = 2.25$, but it remains small as compared with the total dissipation.

Figure 12 shows the normalized dilatation dissipation for $Ma = 2.25$ and $Ma = 6$, where $\varepsilon_d = 4/3\bar{\mu}\overline{(\partial u_i''/\partial x_i)^2}$. Both the dilatation dissipation and the pressure dilatation are proper measurement of the compressibility effects. From this figure we can see that the normalized ε_d for $Ma = 6$ is much larger than that for $Ma = 2.25$. However, ε_d is very small, and in general is less than 0.4% of the total dissipation.

Extended self-similarity (ESS) is an important development in the study of turbulence. According to ESS, the pth order velocity structure function $\langle|v(x+l) - v(x)|^p\rangle$ follows an exponent function of the 3rd order velocity function. ESS is thought to hold in full-developed isotropic turbulence, but it is found in this study that ESS also holds in well turbulence and even in the near-wall region in the spanwise direction. Figure 13 shows the pth order cross-stream velocity structure function $S_p(k) = \langle|w(z + k\Delta z) - w(z)|^p\rangle$ versus the third-order cross-stream velocity structure function at vertical location $y^+ = 98.4$, and the streamwised location is $x = 9.8$. The lines in Fig. 13 show the linearity in logarithms between $S_p(k)$ and $S_3(k)$. From this figure we can see that the ESS holds true until $k = 50$. This means that the ESS range is $l^+ = 50\Delta z \approx 190$.

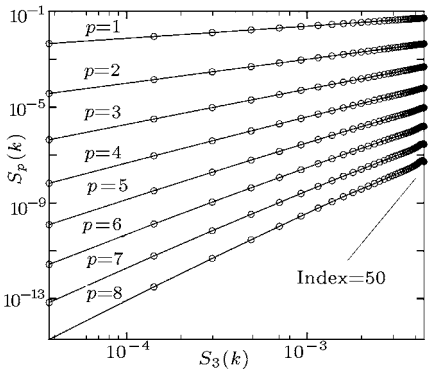

Fig. 13. Behaviour of $S_p(k)$ as a function of $S_3(k)$ at $y^+ = 98.4$, $x = 9.8$.

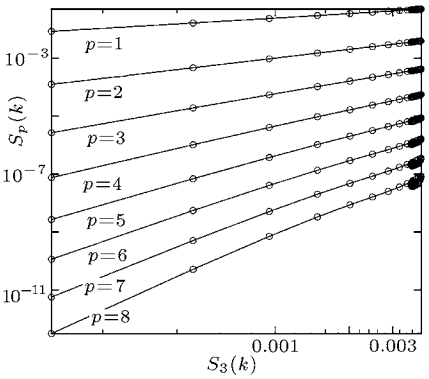

Fig. 14. Behaviour of $S_p(k)$ as a function of $S_3(k)$ at $y^+ = 5.2$, $x = 9.8$.

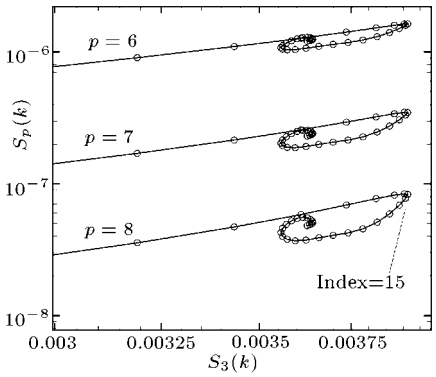

Fig. 15. Detail of Fig. 14.

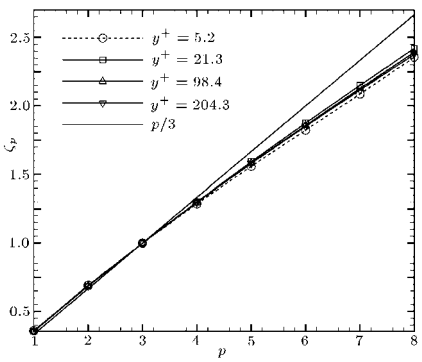

Fig. 16. Relative scaling exponents.

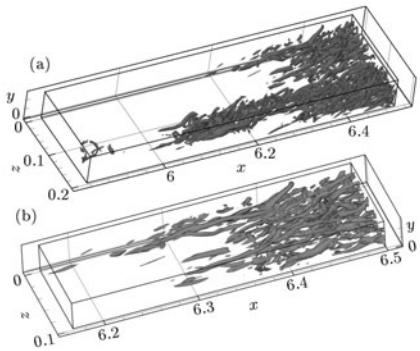

Fig. 17. (a) Instantaneous isosurface of $Q^+ = 0.005$, $Ma = 6$. (b) Detail.

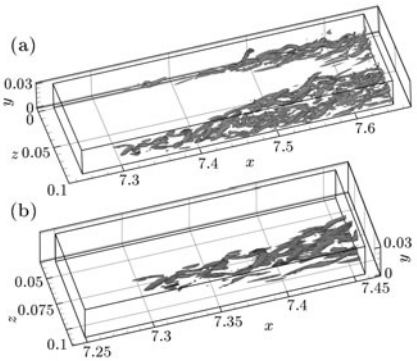

Fig. 18. (a) Instantaneous isosurface of $Q^+ = 0.005$, $Ma = 2.25$. (b) Detail.

Figure 14 shows $S_p(k)$ as a function of $S_3(k)$ in the near-wall region $y^+ = 5.2$ (the streamwised location is $x = 9.8$), with its enlarged picture given in Fig. 15. From Figs. 14 and 15 we can see the linear dependence region extends to $k = 15$. This means that ESS holds in the range $l^+ = 15\Delta z \approx 57$, about half the width of near-wall streaks. Because of the near-wall streak influence, the ESS range is much narrower in the near wall region. Figure 16 shows the relative scaling exponents calculated by using the least-square-fit method from the ESS lines. From this figure, we can see that the exponents in the near-wall region ($y^+ = 5.2$) are a little lower than those at other locations, and this agrees with the experiment results of Ref. [9].

Figure 17(a) shows the instantaneous isosurface of $Q^+ = 0.005$, where $Q^+ = Q/(u_\tau/l^*)^2$, Q is the second invariant of the velocity gradient tensor, u_τ and l^* are the wall friction velocity and wall unit at $x = 9.8$, respectively. The partial enlarged figure is given in Fig. 17(b). Figures 18(a) and 18(b) show the instantaneous isosurface of $Q^+ = 0.005$ for the turbulent boundary layer with $Ma = 2.25$.[6] In comparison with the case of $Ma = 2.25$, we can see that the coherence vortices are arranged to be smoother and streamwised, and the hair-pin vortices are less occurred in the high Mach number flow.

In summary, DNS of a spatially evolving supersonic turbulent boundary layer at $Ma = 6$ has been performed by using the 7th order WENO scheme combined with the 8th order central scheme.

The authors would like to thank the State Key Laboratory of Scientific and Engineering Computing (LSEC) and Supercomputing Centre of Chinese Academy of Sciences (SCCAS) for providing computer time. The authors would like to thank Professor Zhou Heng and Professor Luo Jisheng of Tianjin University for helpful discussion.

References

[1] Guarini S E, Moser R D, Shariff K et al 2000 *J. Fluid Mech.* **414** 1
[2] Maeder T, Adams N A and Kleiser L 2001 *J. Fluid Mech.* **429** 187
[3] Huang Z F, Zhou H and Luo J S 2005 *Sci. Chin.* G **48** 626
[4] Rai M M, Gatski T B and Erlebacher G 1995 *AIAA Paper* 95-0583
[5] Priozzoli S and Grasso F 2004 *Phys. Fluids* **16** 530
[6] Gao H, Fu D X, Ma Y W and Li X L 2005 *Chin. Phys. Lett.* **22** 1709
[7] Jiang G S and Shu C W 1996 *J. Computat. Phys.* **126** 202
[8] Huang Z F, Cao W and Zhou H 2005 *Sci. Chin.* G **48** 614
[9] Jiang N and Zhang J 2005 *Chin. Phys. Lett.* **22** 1968